ISSN 2433-2224(Online)
JAXA-RM-18-001E

JAXA Research and Development Memorandum

Low-Boom and Low-Drag Design of Small Supersonic Transport Considering Propulsion Airframe Integration

Atsushi UENO and Yoshikazu MAKINO

October 2018

Japan Aerospace Exploration Agency

Contents

Low-Boom and Low-Drag Design of Small Supersonic Transport Considering Propulsion Airframe Integration

Atsushi UENO[*1], Yoshikazu MAKINO[*1]

ABSTRACT

Japan Aerospace Exploration Agency (JAXA) has conducted a low-boom and low-drag design considering propulsion airframe integration for a 50-seat-class supersonic transport. In this study, three technical targets in terms of airport noise, lift-to-drag ratio, and sonic boom were defined. Design results complying with three technical targets are summarized in this paper. First, engine specifications are optimized to comply with ICAO noise standards. In this optimization, only the engine (jet) noise is considered, and the engine exhaust velocity that has strong impact on jet noise is constrained. The objective function to be maximized is the range performance. Then, the engine nacelle is designed based on the optimized engine specifications and is integrated with the low-boom-designed airframe considering range performance and sonic boom loudness. Finally, technical targets on lift-to-drag ratio and sonic boom are validated by the Navier-Stokes analysis and wind tunnel tests.

Keywords: Supersonics, Low-boom, Propulsion airframe integration

1. Introduction

Japan aerospace exploration agency (JAXA) has conducted the Silent SuperSonic (S3) program from 2006 to 2015 in order to obtain key technologies realizing an environmentally friendly and economically viable supersonic transport. The British-French commercial supersonic transport 'Concorde' had drawbacks regarding environmental acceptability and economic efficiency. In this program, four technical targets were set in order to improve them as follows: a) the sonic boom overpressure is decreased by half (overpressure < 0.5 psf) as compared to the Concorde technology (i.e., the N-wave sonic boom), b) the airport noise is decreased to comply with ICAO noise standards (Chapter 4), c) the cruise lift-to-drag ratio is improved to 8, and d) the structural weight is decreased by 15% as compared to the Concorde technology. To achieve these targets, research and development on element technologies was conducted. Results were applied to the conceptual design of a small sized supersonic transport. Numerical analyses and wind tunnel tests were performed for the conceptual design results to validate applied element technologies. In this paper, results of the conceptual design considering technical targets except for that of the structural weight is summarized with a focus on propulsion airframe integration.

Specifications in the conceptual design is shown in Table 1.1. A small sized (50-seat-class) twin-engine jet is the design target, aiming at early entry into service in the near future. The aircraft weight is set to 70 ton considering the aircraft size and the technical target of structural weight. Range target is 3,500 nm that enables an one-day business trip from Japan to major cities in Asian countries. This target also enables trans-Pacific flights. The cruise Mach number is set to 1.6, because the cruise speed should be at least doubled as compared to existing subsonic aircrafts to ensure operational benefits for airline companies.

Table 1.1 Specifications of 50-seat-class supersonic aircraft

Passengers	50
Length	53 m
Wing area	175 m^2
Weight (Fuel weight)	70 ton (34 ton)
Engine	Twin-engine
Cruise speed	1.6 Mn
Range	3500 nm

First, a low-boom and low-drag design is performed for a glider configuration without a propulsion system (Section 3). Then, engine specifications that can comply with ICAO noise standards (Chapter 4) are optimized, and the optimized propulsion system is integrated with the glider configuration designed in Section 3 considering sonic boom loudness and

* Received July 25, 2018
*1 Aviation Systems Research Unit, Aeronautical Technology Directorate

range performance (Section 4). Finally, numerical analyses and wind tunnel tests are performed for the designed configuration in order to validate the technical target of low-drag and low-boom (Section 5).

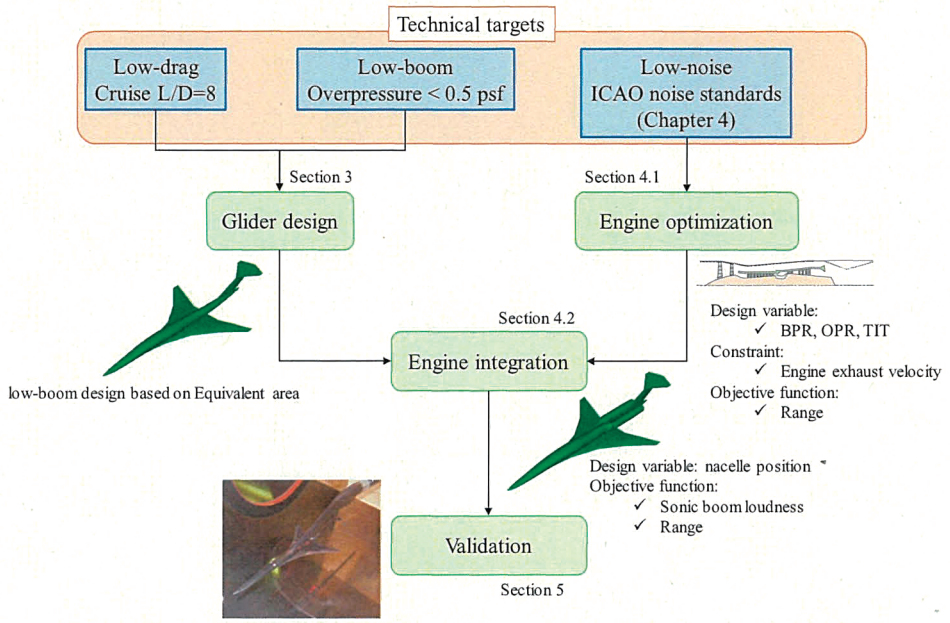

Fig. 1.1 Conceptual design with focus on propulsion airframe integration.

2. Design tools [2.1)]

Low-boom design tools developed by JAXA are summarized in this section. JAXA's low-boom design is divided into two phases. In the first phase, low-fidelity design tools are used, and an initial shape is defined considering a wide range of design space. In the second phase, high-fidelity design tools are used, and an initial shape is refined in a narrow design space as compared to the first phase.

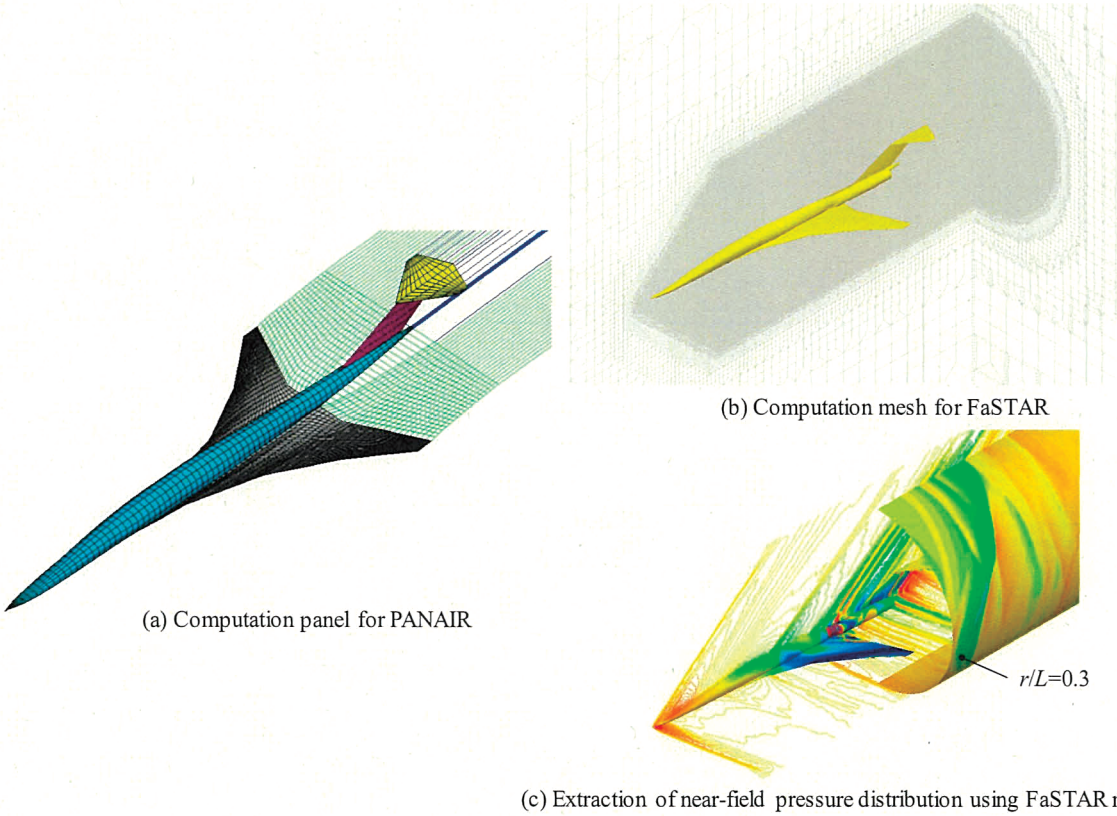

(a) Computation panel for PANAIR

(b) Computation mesh for FaSTAR

(c) Extraction of near-field pressure distribution using FaSTAR result

Fig. 2.1 JAXA's low-boom design tools

As a low-fidelity design tool, 'CAPAS' [2.2] developed by JAXA is used. CAPAS enables automatical shape definition for wing-body-tail configurations without engine nacelles in cooperation with the commercial CAD software 'CATIA V5', and computational panels are automatically generated for aerodynamic analyses conducted by the linear potential code 'PANAIR (A502)' [2.3]. PANAIR provides near-field pressure distributions that are extracted on a cylinder surface with a radius (r) equal to a fuselage length (L) (i.e., r/L=1). However, there are two points of issue on these near-field pressure distributions: 1) non-linear effects are not considered in the PANAIR analysis, and 2) the near-field cylinder radius (r/L=1) may not large enough to capture three-dimensional effects in a flowfield. First, near-field pressure distributions are modified by the area balancing method used in the F-function method [2.4] in order to consider non-linear effects. Second, the multipole analysis [2.5), 2.6)] is introduced to capture three-dimensional effects, and near-field pressure distributions are modified again considering pressure propagation in the circumferential direction. Modified near-field pressure distributions are used as an input to the far-field propagation analysis. JAXA developed 'Xnoise' [2.7] for this propagation analysis. Xnoise is based on the augmented Burgers equation and gives sonic boom signatures on the ground. The reflection factor on the ground is assumed to be 1.9. Finally, the sonic boom loudness is computed using JAXA's BoomMetre [2.1] in terms of Steven's Mk VII perceived level (PL) [2.8].

For high-fidelity analyses in the second design phase where engine nacelles are modeled, the automatical mesh generator 'HexaGrid' [2.9] and Navier-Stokes solver 'FaSTAR' [2.10], both of which are developed by JAXA, are used instead of CAPAS and PANAIR. HexaGrid generates hexahedral computation grids automatically for Navier-Stokes and Euler analyses conducted by FaSTAR. Near-field pressure distributions are extracted on a cylinder surface with a radius of 0.3L (r/L=0.3). These pressure distributions are modified by the multipole analysis. Then, the far-field propagation analysis and the evaluation of sonic boom loudness are performed by Xnoise and BoomMetre, respectively. When FaSTAR is used as an Euler solver, the skin friction drag is evaluated using the skin friction coefficient for flat plate [2.11] and is added to pressure drag to give lift-to-drag ratio.

3. Glider design [3.1]

The low-boom and low-drag design of the glider (wing-body-tail) configuration using low-fidelity design tools is summarized in this section. Design conditions are Mach number of 1.6, lift coefficient referred to the wing area (175 m^2) of 0.15, and flight altitude of 14.6 km. The low-drag design is performed mainly for the wing, and its twist and camber are optimized. The low-boom design is performed mainly for the fuselage and the horizontal tail considering the equivalent area distribution. In order to decrease the sonic boom overpressure by half as compared to the N-wave sonic boom, the target equivalent area distribution is defined so that front and aft booms are fragmented into double shock waves (Fig. 3.1). In Fig. 3.1, the reversed equivalent area [3.2] is shown. For reduction of the front boom overpressure, the cross-section area distribution of the fuselage is designed so that the shock waves of the nose and the wing leading edge are kept isolated (Fig. 3.1 and 3.2). For reduction of the aft boom overpressure, the t-tail configuration is selected (Fig. 3.3), and the aft boom is fragmented into double shock waves by the horizontal tail (Fig. 3.1 and 3.2).

Regarding the target equivalent area distribution (Fig. 3.1), results of high-fidelity analysis are considered, as shown below. In the S3 program, the initial shape design using low-fidelity design tools and its refinement using high-fidelity design tools considering the nacelle integration were conducted sequentially. Before the refinement of the initial shape, the high-fidelity analysis was performed for the initial shape with side-body nacelles shown in the next chapter. Results showed that the aft boom has single shock wave (i.e., the N-wave), though that of the initial shape without side-body nacelles is fragmented into double shock waves. This difference is caused mainly by the difference of configuration fidelity. The high-fidelity analysis shows the expansion wave caused by the nacelle that is not modeled in the PANAIR analysis (Fig. 3.4). This expansion wave has strong impact on the aft boom, causing lower minimum pressure than that of the PANAIR analysis, which means that the strength of the t-tail shock wave required to the aft boom fragmentation is underestimated by the PANAIR analysis. Thus, the strength of the t-tail shock wave required to the aft boom fragmentation was estimated considering the nacelle expansion wave obtained by the high-fidelity analysis, and the low-fidelity low-boom design was performed to meet this requirement (Fig. 3.1).

In this low-fidelity design, the parametric study is performed for the horizontal tail of the baseline configuration (Fig. 3.3) considering 5 parameters (thickness to chord ratio, camber, elevator angle, sweep back angle of leading edge, and root chord length). In this parametric study, the lift coefficient is constrained at 0.15 (the design lift coefficient), while the longitudinal trim condition is not constrained. Changes of drag coefficient, aft boom signature, and position of center of pressure are examined. As a result, the extended root chord and the negative camber show reduction of the aft boom overpressure and also show less impact on the drag coefficient and the position of center of pressure. The extended root chord increases the shock wave strength, which is desirable to the aft boom fragmentation. At the same time, it has little impact on the drag coefficient, because the thickness to chord ratio is fixed at 3%. The negative camber also increases the shock wave strength. However, it increases drag and causes lift reduction that changes the position of center of pressure. The root chord length and the negative camber are designed considering the best compromise between these advantage and disadvantage (Fig. 3.3).

Then, the low-fidelity low-drag design is performed for the wing, and its twist and camber are optimized. In this optimization, objective functions are the drag coefficient and the sonic boom loudness at the design lift coefficient. The elevator angle is set to realize longitudinal trim condition considering the position of the center of gravity (Fig. 3.3).

High-fidelity analyses for the designed glider configuration (Fig. 3.3) are conducted. As seen in the ground sonic boom signature (Fig. 3.2), front and aft booms are successfully fragmented into double shock waves. Its sonic boom loudness is 96.0 PLdB.

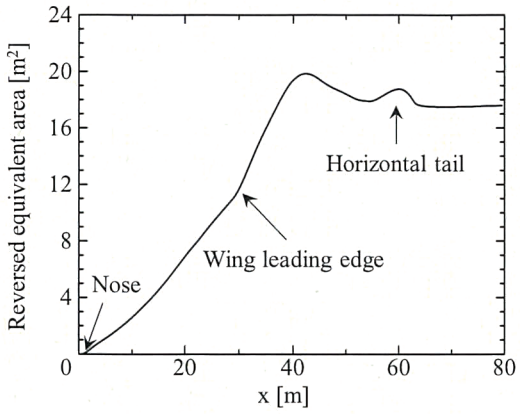

Fig. 3.1 Reversed equivalent area distribution

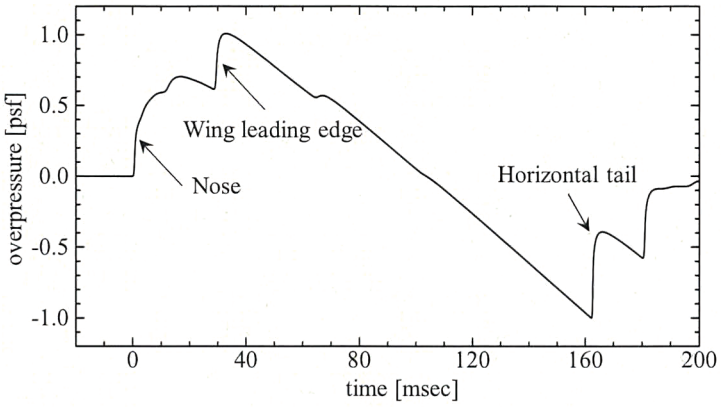

Fig. 3.2 Ground sonic boom signature

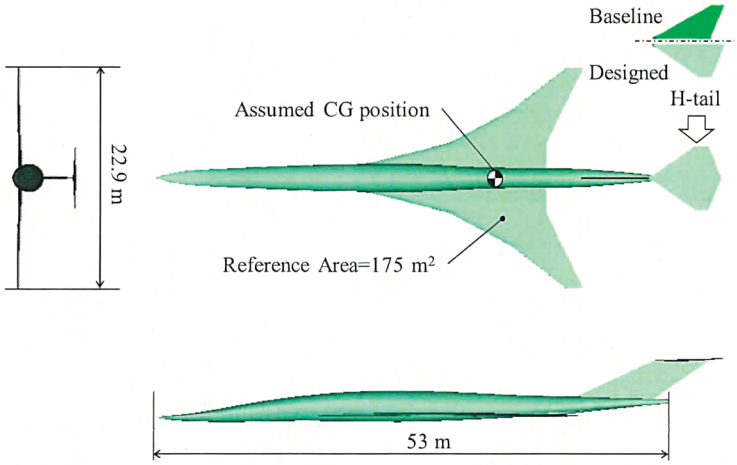

Fig. 3.3 Glider configuration

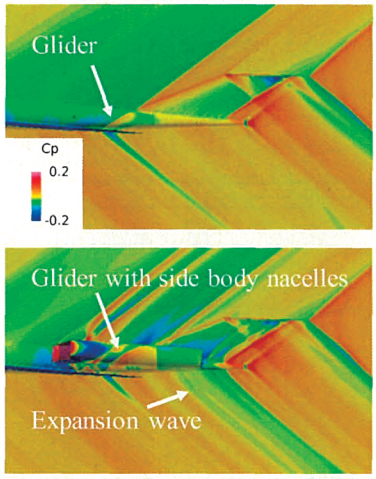

Fig. 3.4 Effect of nacelle integration on flowfield [3.1)]

4. Engine integration

4.1. Engine specifications complying with airport noise standards [4.1)]

Airport noise of a supersonic transport can be assumed to depend largely on engine specifications, because supersonic engines have a smaller bypass ratio and produce larger engine (jet) noise than subsonic engines. Therefore, engine specifications are optimized to comply with ICAO noise standards (Chapter 4). In order to estimate airport noise, an acoustic analysis should be conducted considering take-off and landing trajectories, flight velocity, thrust setting, and so on. In this study, engine specifications are optimized under a constraint on an engine exhaust velocity without conducting an acoustic analysis, because an engine exhaust velocity has a strong impact on airport noise [4.2)]. The constraint value of engine exhaust velocity was determined based on a discussion with engine company, though the constraint value is not specified in this paper. Design parameters in this study are the bypass ratio (BPR), the overall pressure ratio (OPR), and the turbine inlet temperature (TIT).

The engine is the fixed cycle, mixed-flow, two-shaft turbofan engine without reheat. The variable convergent-divergent nozzle is installed. Only the divergent flap is variable. The required thrust is shown in Table 4.1. The required thrust at the supersonic cruise is set at 4.5 ton considering the aircraft weight (70 ton), the target lift-to-drag ratio at supersonic cruise (8), and the excess thrust. Before determining the required take-off thrust, the thrust-to-weight ratio is examined. Based on the required climb gradient at the second take-off segment (2.4% for twinjets) and the target lift-to-drag ratio at the take-off (6.2), the thrust-to-weight ratio is set at 0.43. As a result, the required take-off thrust becomes 15 ton. Finally, the required thrust at the transonic climb speed (Mach 0.9) is set at 3.6 ton considering the excess thrust.

The engine performance data such as the specific fuel consumption (SFC) is calculated by the thermodynamic cycle analysis. At given BPR, OPR, and TIT, this analysis is conducted, and engine design parameters such as the fan diameter are defined to meet required thrust. Design ranges of BPR, OPR, and TIT were determined based on a discussion with

engine company, though they are not specified in this paper. The thermodynamic cycle analysis is performed in this design space, and the engine database including the SFC, the engine weight, and the engine exhaust velocity at take-off are constructed. Here, the SFC is calculated at the five design points shown in Table 4.1.

Table 4.1 Required thrust per engine [4.1)]

Flight conditions		Required thrust
Take-off	Sea level/0.0 Mn	15 ton
Supersonic cruise	50 kft/1.6 Mn	4.5 ton
Acceleration/climb	40 kft/0.9 Mn	3.6 ton
Acceleration/climb	45 kft/1.2 Mn	n/a
Subsonic cruise	30 kft/0.9 Mn	n/a

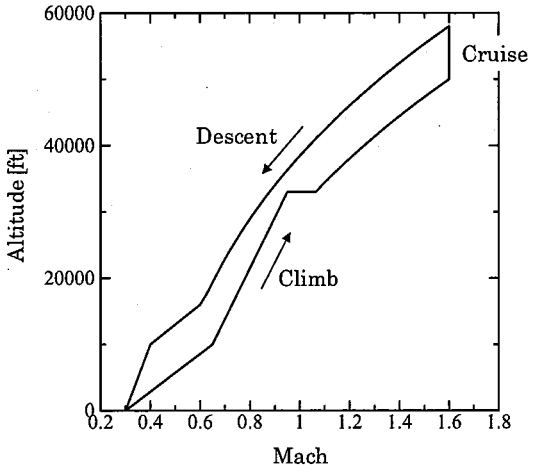

Fig. 4.1 Flight trajectory

The mission performance analysis is conducted and the optimum engine specifications are explored to maximize the range performance under the constraint on the engine exhaust velocity at take-off. The flight trajectory for this analysis is shown in Fig. 4.1. The engine thrust and SFC are given at 5 points shown in Table 4.1. However, the engine data providing the engine thrust and SFC at arbitrary points along the flight trajectory is needed for the mission performance analysis. In this study, the engine data for the previous conceptual design of a supersonic business jet is tailored considering the thrust and SFC at 5 design points shown in Table 4.1. As for the aerodynamic data, the lift-to-drag ratio at the cruise Mach number is fixed at 8 (i.e., the technical target), though it is affected by engine specifications such as the fan diameter. The aerodynamic data at other Mach numbers is also assumed to be independent of engine specifications and is determined considering the lift-to-drag ratio used for the previous conceptual design of a supersonic aircraft.

The flow diagram of the mission performance analysis is shown in Fig. 4.2. First, engine specifications (BPR, OPR, and TIT) are set, and the engine performance data (thrust and SFC at 5 design points, engine weight, and exhaust velocity at take-off) is obtained from the engine database constructed by the thermodynamic cycle analysis. The take-off weight is the sum of the engine weight, fuel weight (33.8 ton), and zero fuel weight (26.2 ton). The range performance is estimated using the energy method and the Breguet range equation [4.3)]. As mentioned above, the airport noise depends only the engine exhaust velocity in this study.

Results of the range estimation are shown in Fig. 4.3, showing contour plots of the range performance. The range performance is normalized so that the range performance becomes unity when BPR, OPR and TIT have the minimum value in the design space. In this study, constraints are imposed on the load of high-pressure turbine in order to avoid large changes in the efficiency of high-pressure and low-pressure turbines. They are not satisfied in the shadowed area in Fig. 4.3. When TIT is the maximum in the design space, the dotted line can be seen in the right figure of Fig. 4.3. In the area on the right side of the dotted line, the constraint on the airport noise (i.e., the engine exhaust velocity at take-off) is satisfied. When TIT is the minimum in the design space, the constraint on the airport noise is satisfied in the all region in the left figure of Fig. 4.3. The range performance becomes the maximum at the point A, however the constraint on the airport noise is not satisfied. The best compromise between the range performance and the airport noise can be seen at the point B. When TIT is the minimum, the range performance becomes the maximum at the point C. Effects of engine specifications on the range performance and the airport noise are summarized as follows.

The effect of TIT; As TIT becomes high, the thermal efficiency is improved. As a result, the core engine becomes small, and the engine weight is reduced. SFC is also improved owing to high TIT. Thus, the range performance is improved as TIT becomes high.

The effect of BPR; As BPR becomes large, SFC is improved. At the same time, the engine weight is increased because

of the large fan diameter, which degrades the range performance. On the other hand, the engine exhaust velocity is increased as BPR becomes small. When TIT is the maximum in the design space, the point A showing the maximum range performance cannot be selected due to violation of the constraint on the airport noise. Increasing BPR reduces the airport noise but degrades the range performance. Thus, BPR should be set considering the trade-off between the range performance and the airport noise.

The effect of OPR; OPR has little impact on the range performance and the airport noise. Increasing OPR slightly improves the range performance and slightly reduces the airport noise.

Based on the above discussion, the point B, where the range performance is maximized under the constraint on the airport noise, is selected. The fan diameter is 1.7m. The engine weight is 6.6 ton, and the take-off weight is 66.6 ton. The selected engine is referred to as the reference engine in the following sections. It should be noted that the supersonic cruise condition is the design condition in the thermodynamic cycle analysis. It means that TIT becomes the maximum not at take-off but at supersonic cruise.

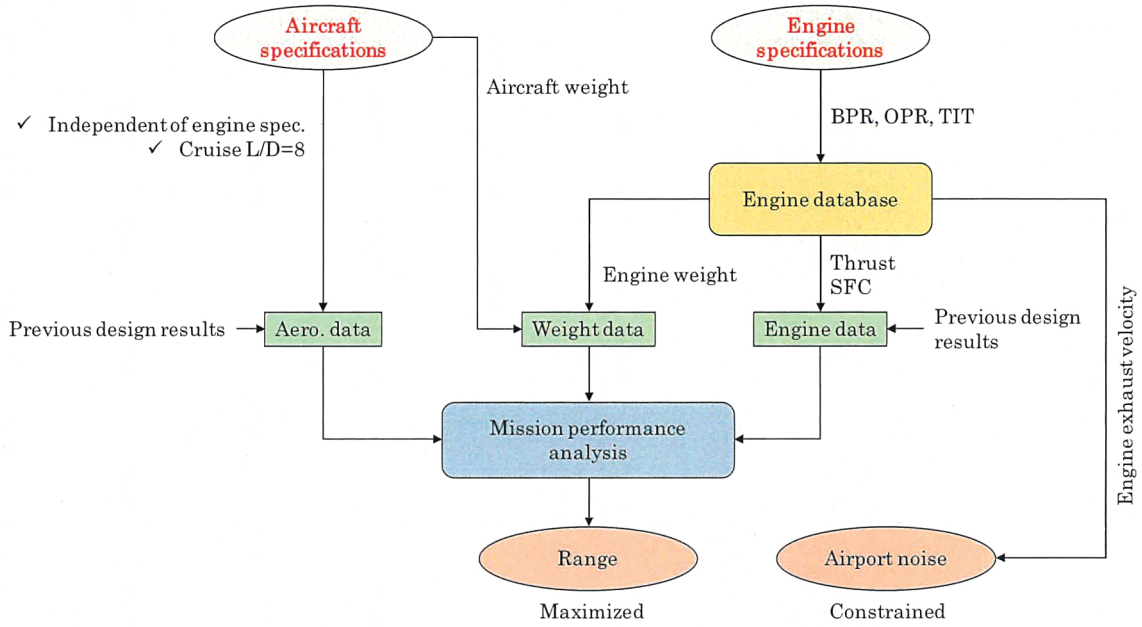

Fig. 4.2 Flow diagram of mission performance analysis [4.1)]

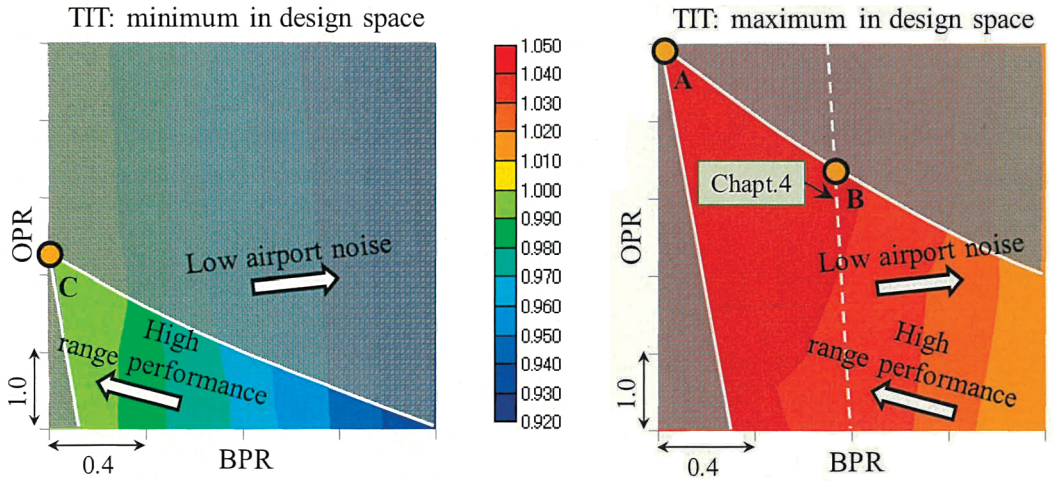

Fig. 4.3 Contour plots of range performance [4.1)]

4.2. Engine integration considering sonic boom and range performance [4.4, 4.5)]

The intake and nacelle geometries are designed for the reference engine using the design tool [4.6)] developed by JAXA in the development of JAXA's Silent SuperSonic Technology Demonstrator (S3TD). The intake is the two-stage, external compression intake with side plates. Designed nacelles are integrated with the glider similar to the optimized glider described in Section 3. Its front and aft booms are fragmented into double shock waves, and the sonic boom loudness is

97.1 PLdB.

The nacelle position is optimized with objective functions of the sonic boom loudness and the range performance. In the optimization study, three-types of nacelle layout (i.e., over-wing, under-wing, and side-body nacelles) are considered. Typical nacelle positions are shown in Fig. 4.4. The design variable is the nacelle position (Table 4.2 and Fig. 4.5) that is represented by the center of intake throat.

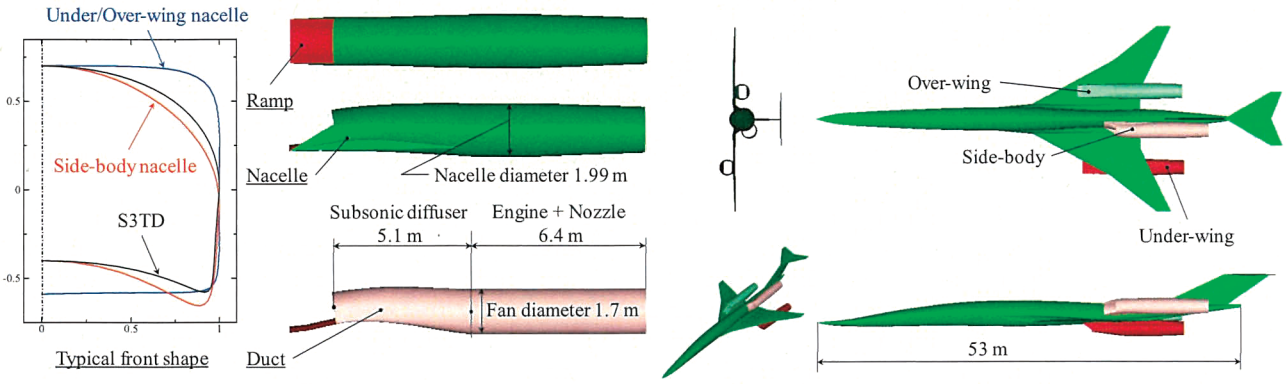

Fig. 4.4 Typical nacelle geometry and nacelle positions [4.4)]

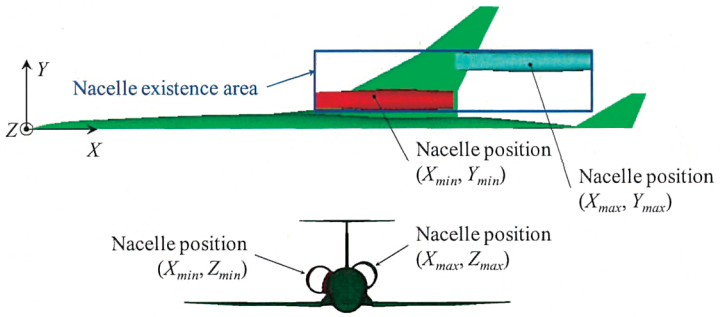

Fig. 4.5 Design variable [4.4)]

Table 4.2 Design variable [4.4)]

Over/under-wing		Side-body	
Xmin	28.514 m	*Xmin*	28.514 m
Xmax	41.508 m	*Xmax*	41.508 m
Ymin	2.756 m	*Zmin*	1.908 m
Ymax	6.360 m	*Zmax*	2.332 m

The local Mach number at the ramp depends on the nacelle position. For example, when the over-wing nacelle is selected, the local Mach number at the ramp is increased by the expansion wave on the wing, and the ramp angle should be increased to decelerate the captured flow. Thus, the ramp angle is adjusted for each nacelle position. In the adjustment, two constraints are imposed as follows; 1) the Mach number in front of the terminal shock wave should be less than 1.3 in order to avoid the boundary layer separation behind the terminal shock wave, and 2) the triple point of the shock wave system on the ramp should be positioned close to the intake lip. The diverter height is determined based on the boundary layer thickness at the ramp. Though the boundary layer thickness at the ramp depends on the nacelle position, the diverter height is fixed at 102 mm during the optimization of nacelle position. For this diverter height, the intake aerodynamic performance, that is the pressure recovery ratio, is no lower than 90% even when the boundary layer at the ramp becomes the thickest. When the ramp is positioned in front of the wing leading edge, the diverter is not installed. The intake front shape (Fig. 4.4) is determined by the Bezier curve. It also depends on the nacelle position, and control points of the Bezier curve are adjusted for each nacelle position so that the ramp shape is fitted to the airframe or wing shape.

The objective functions in this optimization study, which are evaluated assuming the flow-through nacelle, are the sonic boom loudness and the range performance. The sonic boom loudness is represented by the difference from that of the glider without nacelles (i.e., 97.1 PLdB). The range performance is evaluated using only the Breguet equation, which differs from the method described in Section 4.1. Here, the flight phases other than the cruise phase (e.g., the climb phase) are not considered in the Breguet equation. Thus, the range performance is represented by 70% of the range obtained by the Breguet equation.

In order to perform the optimization study, response surfaces of the lift-to-drag ratio, the sonic boom loudness, and the

intake aerodynamic performance (i.e., the pressure recovery ratio) are constructed for the reference engine using the Kriging method. They are evaluated at the design lift condition (i.e., C_L=0.15). For the evaluation of the lift-to-drag ratio and the sonic boom loudness, high-fidelity analysis tools (Euler analysis) explained in Section 2 are used. For the evaluation of the intake aerodynamic performance, Navier-Stokes analysis is conducted [4.6]. The intake aerodynamic performance is represented by the pressure recovery at the fan face. Response surfaces are constructed with 8 initial samples. Then, samples are added based on the probability of improvement [4.7]. Here, the pressure recovery ratio depends on the nacelle position. For example, some of the over-wing nacelles cause boundary layer separation on the intake side wall due to the cross flow over the wing, and intake aerodynamic performance is degraded. As a result, the thrust is decreased, which leads to the increased fan diameter in order to produce the required thrust (4.5 ton) at the supersonic cruise condition. This, in turn, increases the engine weight and degrades the range performance. Thus, the range performance should be evaluated adjusting the fan diameter for each nacelle position. For this purpose, 1) the relation between the pressure recovery ratio and the thrust or SFC, 2) the relation between the fan diameter and the engine weight, and 3) the relation between the fan diameter and the lift-to-drag ratio should be examined. As for the first item, thermodynamic cycle analyses were conducted, which showed that the relation between the pressure recovery ratio and the thrust or SFC is nearly linear. In this study, the linear model, where 1% degradation of the pressure recovery ratio causes 1.47% reduction in the thrust and 0.57% degradation of SFC, is applied. As for the second item, the engine weight is assumed to be proportional to the square of the fan diameter. Finally, the nacelle drag coefficient is increased or decreased by 3 drag count by 0.15 m increase or decrease in the fan diameter. This model is based on CFD results for over-wing nacelles having different fan diameter. The diverter drag coefficient is set at 2 drag count considering experimental results [4.8].

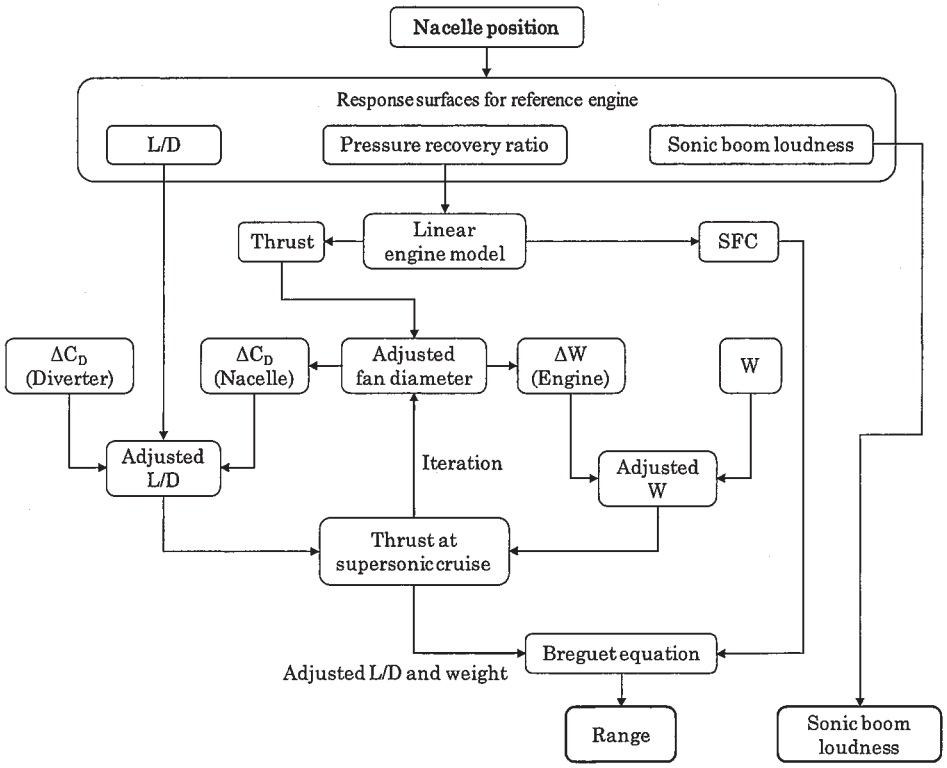

Fig. 4.6 Flow diagram of range evaluation [4.4]

The flow diagram of range evaluation in the optimization study is shown in Fig. 4.6. First, a lift-to-drag ratio and a pressure recovery ratio are obtained from response surfaces for the reference engine. Then, an initial assumed value is given to the fan diameter, and corresponding changes in the nacelle drag and the engine weight from the reference engine are calculated using the linear engine model mentioned above. The lift-to-drag ratio and the weight is adjusted considering these changes. When the diverter is installed, the diverter drag is added. The required thrust at the supersonic cruise is obtained by the adjusted lift-to-drag ratio and weight. The fan diameter is iteratively adjusted to meet this thrust requirement. Finally, the range performance is represented by 70% of the Breguet range. The sonic boom loudness is obtained directly from the response surface and is represented by the difference from that of the glider.

Results of range evaluation are shown in Fig. 4.7. Vertical and horizontal axes show the nacelle position and are normalized by design ranges shown in Table 4.2. Initial 8 sample points '01~08' for the construction of response surfaces are also shown in this figure. Nondominated fronts with respect to the range performance and the sonic boom loudness

are shown in Fig. 4.7 and Fig. 4.8. The nondominated front for under-wing nacelles shows the discontinuity. Whether the diverter drag is added or not is changed discontinuously crossing the wing leading edge, which leads to the discontinuity.

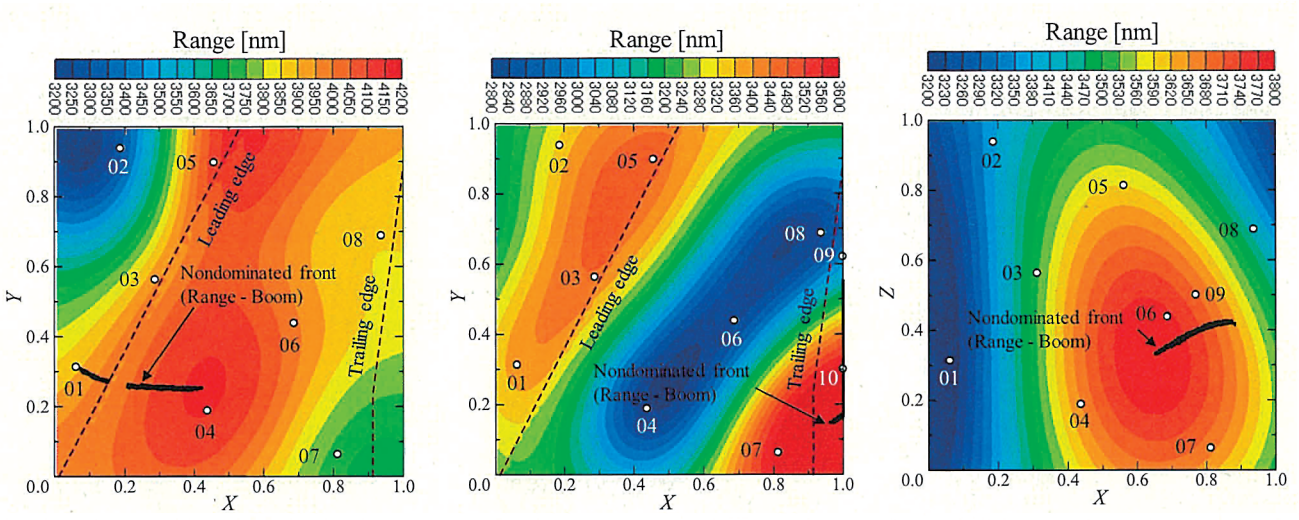

(a) under-wing nacelles (b) over-wing nacelles (c) side-body nacelles

Fig. 4.7 Range performance (optimization of nacelle position) [4.4)]

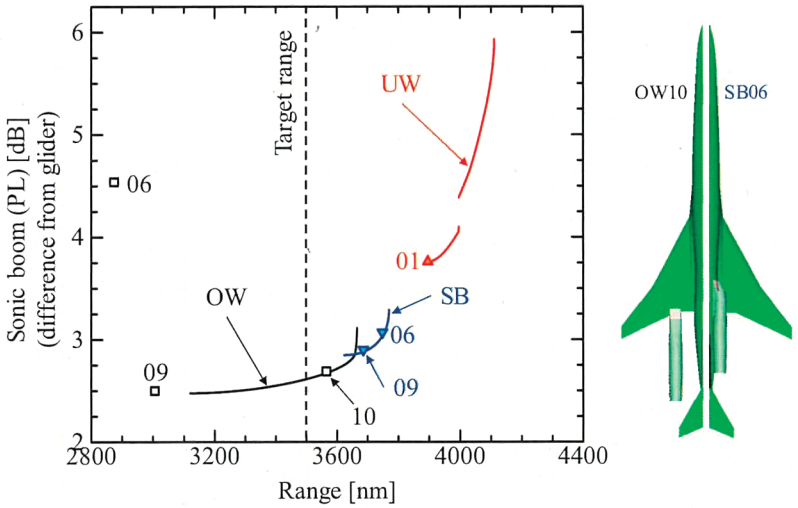

Fig. 4.8 Nondominated front with respect to range and sonic boom loudness [4.4)]

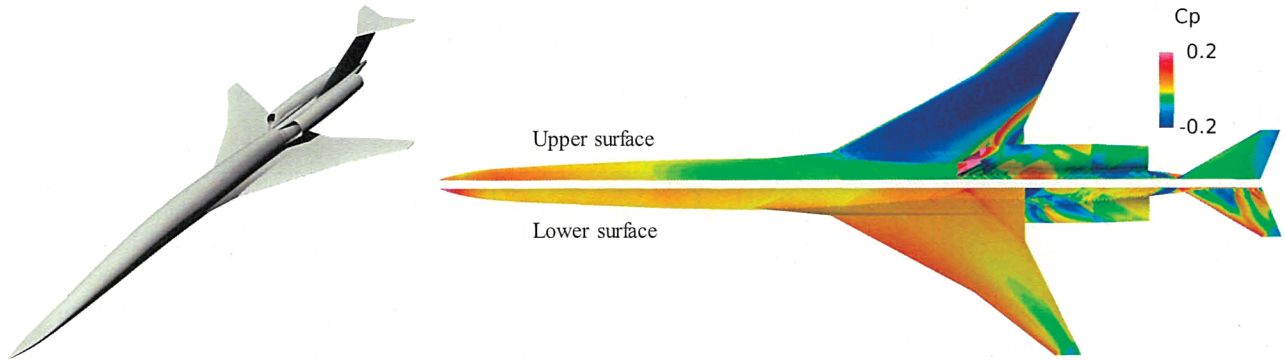

Fig. 4.9 Pressure contour plots for SB06

For under-wing (UW) nacelles, large lift-to-drag ratio is realized due to the compression lift produced by nacelles. The inlet pressure recovery ratio is also large, because the local flow in front of the ramp is pre-compressed by the shock wave at the wing leading edge, and because the stream line under the wing is nearly straight and is parallel to the nacelle axis. Large lift-to-drag ratio and large inlet pressure recovery ratio lead to high range performance as compared to other

nacelle layouts. On the other hand, the sonic boom loudness becomes large due to shock waves at the ramp.

For over-wing (OW) nacelles, negative lift is produced by nacelles, which decreases lift-to-drag ratio. There exists cross-flow over the wing's upper surface, which causes the boundary layer separation on the inlet side wall. As a result, the pressure recovery ratio is degraded. The range performance is also degraded by small lift-to-drag ratio and small pressure recovery ratio. However, the minimum sonic boom loudness is achieved because shock waves at the ramp is shielded by the wing's upper surface and is prevented from propagating to the ground.

For side-body (SB) nacelles, drawbacks mentioned above are overcome. Shock waves at the ramp act only on the wing trailing edge (Fig. 4.9), which reduces negative lift as compared to over-wing nacelles and decreases wing pressure drag at the same time. In addition, shock waves are shielded by the wing's upper surface. Thus, side-body nacelles show good compromise between the range performance and the sonic boom loudness.

At the target range performance (i.e., 3500 nm), the over-wing nacelle shows the minimum sonic boom loudness. However, it is difficult to support engines as shown in Fig. 4.8 (the 10th sample point denoted by OW10). Thus, the 6th sample point for side-body nacelles denoted by SB06 (Fig. 4.8) is selected.

5. Design validation

Nacelles are integrated with the glider shown in Section 3 according to the optimized position described in Section 4.2. In this section, the designed configuration is examined in terms of three technical targets regarding the lift-to-drag ratio, the sonic boom loudness, and the airport noise. As for the airport noise, the engine exhaust velocity was constrained to comply with ICAO noise standards (Chapter 4) as described in Section 4.1, and it can be assumed that the technical target of airport noise is realized. Thus, the lift-to-drag ratio and the sonic boom loudness are validated.

5.1. Low-drag design

The Navier-Stokes analysis for the designed configuration shows that the lift-to-drag ratio at the design lift coefficient (0.15) is slightly less than the target value (8). In order to reduce drag, the area-rule design is applied to the mid-fuselage where the impact on the sonic boom loudness is assumed to be small. In this design, the fuselage cross-section area is reduced with consideration of the cabin layout so that the maximum equivalent area is reduced by $0.5m^2$ (5%). The area-ruled configuration is referred to as PAI (Propulsion Airframe Integration) model. Results of the Navier-Stokes analysis for PAI model is shown in Fig. 5.1. The drag coefficient at the design lift coefficient is 186 drag count, and the technical target of lift-to-drag ratio (L/D>8) is validated by CFD analysis.

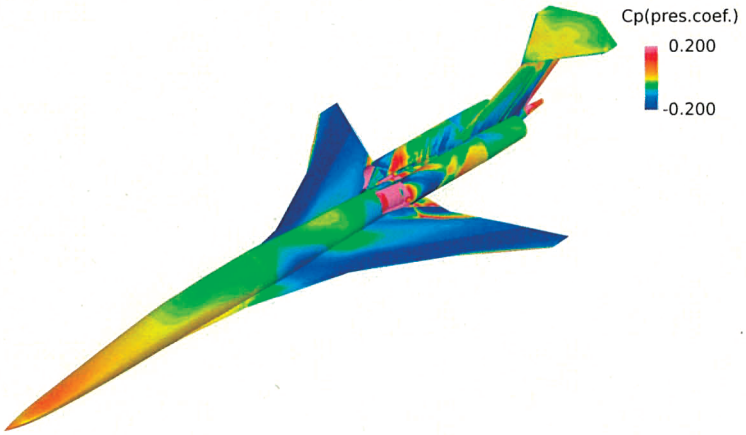

Parts	C_D	$C_{D,\ pressure}$
Fuselage	54	28
Wing	90	56
H tail	12	5
V tail	6	0
Nacelle	23	10
Diverter	1	1
Total	**186**	**100**

Fig. 5.1 CFD results for PAI model

5.2. Low-boom design [3.1)]

The low-boom design is validated by wind tunnel tests conducted at the JAXA 1m x 1m supersonic wind tunnel. The free stream Mach number is 1.6. The unit Reynolds number is 25.5×10^6 [1/m]. The wind tunnel model is 424 mm long and is 0.8% scale of the actual aircraft, which makes it difficult to fabricate nacelles whose thickness is less than 1 mm. Therefore, wind tunnel tests are conducted using the glider model without nacelles. This model is referred to as the wind tunnel test (WTT) model. In wind tunnel tests, near-field pressure distributions are measured and are used to validate results of high-fidelity analyses conducted by FaSTAR. After the validation, the low-boom design of PAI model is validated by FaSTAR.

The WTT model, shown in Fig. 5.2, is supported at the mid fuselage. The model position in the test section is set so that the under-track pressure distribution is measured at r/L of 1 by the 'static pressure rail' having static pressure ports mounted on the lower wall of the wind tunnel. The interval of static pressure ports is 4 mm in the free stream direction.

Fig. 5.2 Wind tunnel model [3.1)]

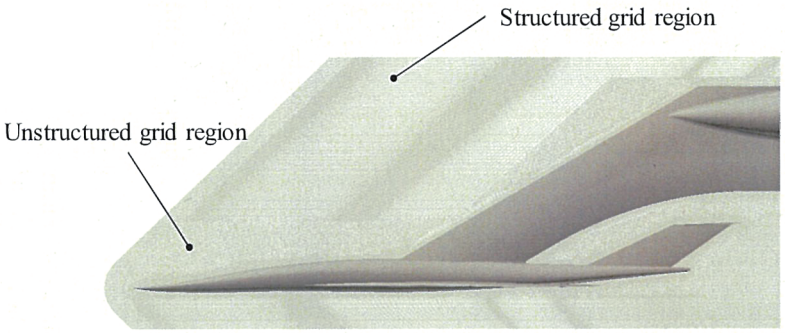

(a) PW-Grid

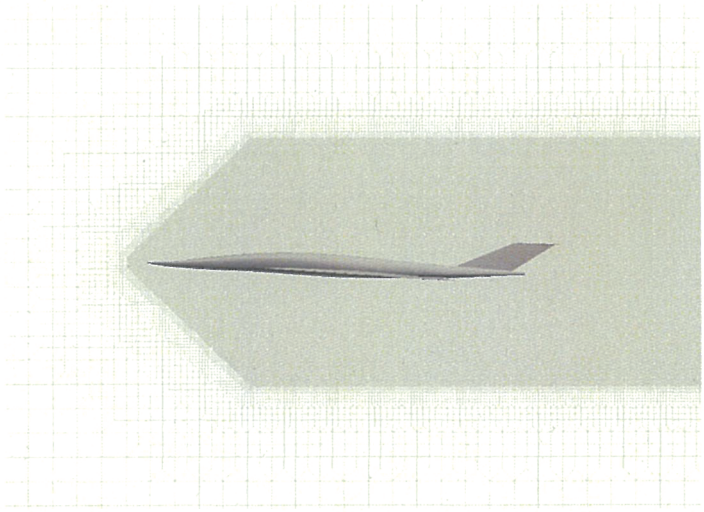

(b) HG-Grid

Fig. 5.3 Computation grids [3.1)]

In order to validate high-fidelity near-field analyses, FaSTAR analyses are conducted and results are compared with wind tunnel results. In the FaSTAR analysis, the boundary layer is assumed to be laminar. The wind tunnel wall and the 'static pressure rail' are not modeled. Therefore, the near-field pressure at the location of 'static pressure rail' is modified considering the reflection factor of 1.9. Instead of HexaGrid described in Section 2, the commercial software 'Pointwise' is used to make computation grids. Here, computation grids made by Pointwise and HexaGrid are referred to as PW-Grid and HG-Grid, respectively. In the PW-Grid, unstructured tetrahedral grids and structured hexahedral grids are generated around the WTT model (Fig. 5.3). At the close proximity of the model, structured 30-layer grids are generated in order to capture the boundary layer. In the structured grid region, fine grids are generated in the region where r/L is smaller than 1.2 and are inclined in order to keep the orthogonality between shock waves and computation grids. On the other hand, HexaGrid produces orthogonal grids, and it is difficult to incline grids. In order to reduce the dissipation, the minimum grid spacing is smaller than that of PW-Grid. As a result, fine grids region of HG-Grid (i.e., $r/L<0.31$) is narrower than that of PW-Grid due to the limitation of computation resources, which makes it difficult to compare results between the

wind tunnel test and the FaSTAR analysis using HG-Grid. Thus, the FaSTAR analysis using PW-Grid is compared with wind tunnel results.

The under-track pressure distribution is shown in Fig. 5.4. Here, p is the static pressure and p_∞ is the static pressure of the free stream. When the sting is modeled in the FaSTAR analysis, pressure distributions of the wind tunnel test and the FaSTAR analysis are quite similar except at the sting position, which shows the reliability of the FaSTAR analysis.

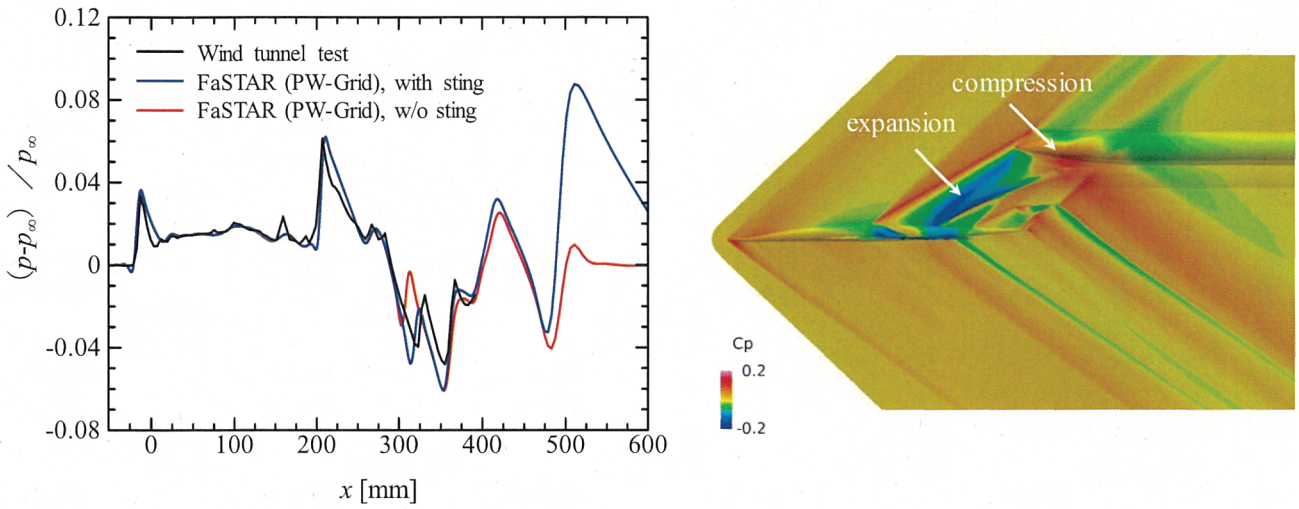

Fig. 5.4 Under-track pressure distributions (comparison between wind tunnel test and FaSTAR with PW-Grid) [3.1)]

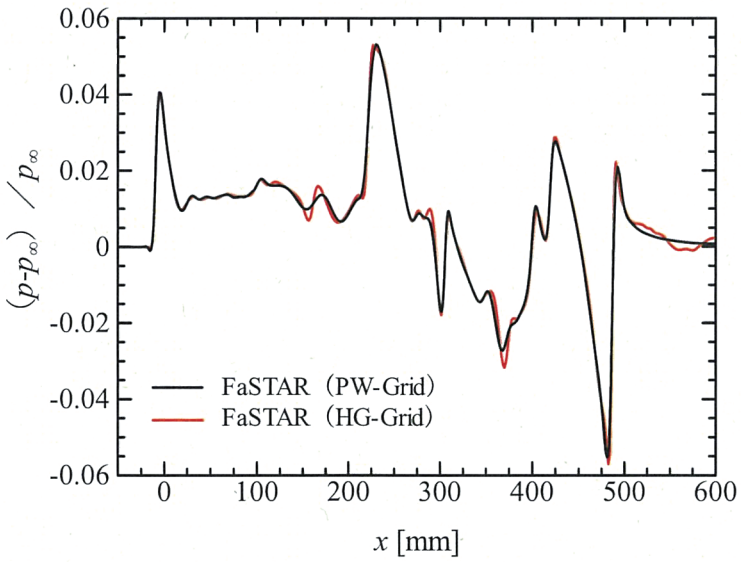

Fig. 5.5 Under-track pressure distributions (comparison between PW-grid and HG-grid) [3.1)]

Before validating the low-boom design of the PAI model using FaSTAR with HG-Grid, near-field pressure distributions obtained by PW-Grid and HG-Grid are compared (Fig. 5.5). Here, r/L is 0.3. They are almost identical. Though the FaSTAR analysis using the HG-Grid is not directly compared with the wind tunnel test, it can be used for the low-boom validation.

The FaSTAR analysis using the HG-Grid is performed for the PAI model, and the obtained near-field pressure distribution (Fig. 5.6(a)) is propagated to the ground (Fig. 5.6(b)) using analysis tools described in Section 2. Both front and aft booms are successfully fragmented into double shock waves, showing that the technical target of the sonic boom loudness (i.e., overpressure of smaller than 0.5 psf) is realized.

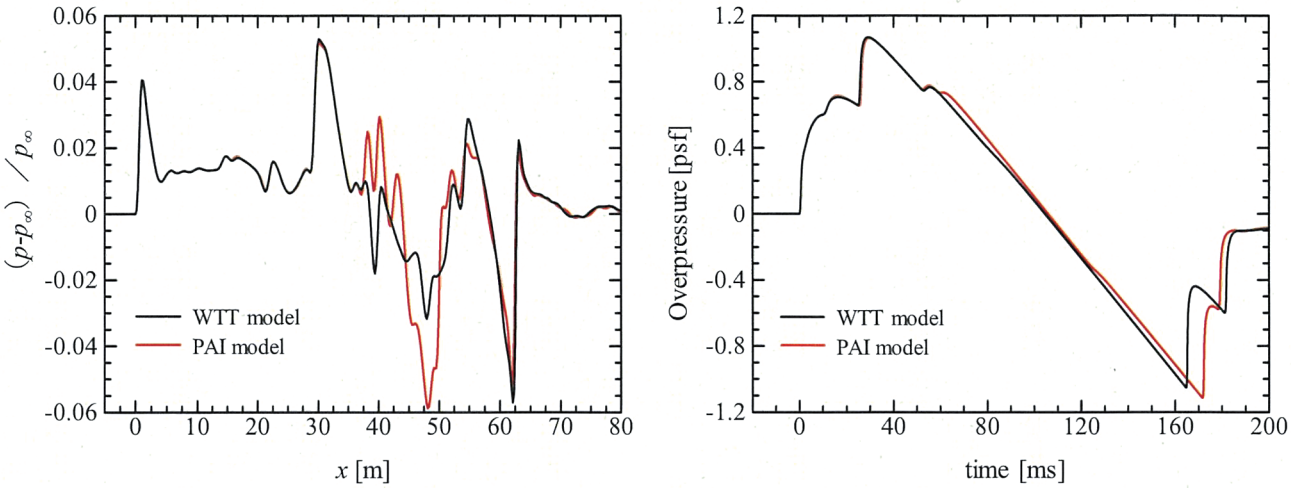

(a) Under-track pressure distributions (b) Under-track sonic boom signatures

Fig. 5.6 Results of sonic boom analysis for PAI model obtained by FaSTAR with HG-Grid [3.1)]

6. Conclusion

Results of low-boom and low-drag design considering propulsion airframe integration conducted by JAXA were summarized. Engine specifications were optimized to maximize range performance under the constraint on the engine exhaust velocity complying with ICAO noise standards (chapter 4). Engine nacelles were designed based on the optimized engine specifications and were integrated with the low-boom-designed airframe. From viewpoints of inlet aerodynamic performance, range performance, and sonic boom, the side-body-nacelle layout was selected. CFD analyses showed that the technical target of lift-to-drag ratio (8) is achieved by the designed configuration. Near-field pressure distributions obtained by CFD analyses that were validated by wind tunnel tests were propagated to the ground. The ground sonic boom signature showed two-stage pressure jump in both front and rear booms, complying with the technical target of sonic boom.

After the S3 program was completed, JAXA started the S4 (System integration of Silent SuperSonic airplane technologies) program (from 2016 to 2019) focusing on the integrated design. The propulsion airframe integration will be investigated further including the effect of exhaust plume on low-boom design. The integration of low speed performance and cruise performance (i.e., the integration of high-lift device and natural laminar flow wing) will be investigated. The flight demonstrator will be planned for the validation of the integrated design.

REFERENCE

2.1) Makino, Y., Naka, Y., Hashimoto, A., Kanamori, M., Murakami, K., and Aoyama, T. : Sonic Boom Prediction Tool Development at JAXA, Aeronautical and Space Sciences Japan, 61, 7 (2013), pp. 237-242. (in Japanese)

2.2) Makino, Y. and Makimoto, T. : Development of CAPAS, conceptual design tool for supersonic aircraft, JAXA-SP-08-009, 2009. (in Japanese)

2.3) Carmichael, R. I. and Erickson, L. I. : PANAIR – A Higher Order Panel Method for Predicting Subsonic or Supersonic Linear Potential Flows about Arbitrary Configurations, AIAA Paper 81-1255, 1981.

2.4) Whitham, G. B. : The Flow Pattern of a Supersonic Projectile, Communications in Pure and Applied Mathematics, 5 (1952), pp. 301-348.

2.5) Page, J. A. and Plotkin, K. J. : An Efficient Method for Incorporating Computational Fluid Dynamics into Sonic Boom Prediction, AIAA Paper 91-3275, 1991.

2.6) Kanamori, M., Hashimoto, A., Aoyama, T., Makino, Y., Ishikawa, H., Yamamoto, M., and Iimura, T. : Improvement of near-field waveform from supersonic vehicle using multipole analysis, JAXA-SP-13-011, 2014. (in Japanese)

2.7) Yamamoto, M., Hashimoto, A., Takahashi, T., Kamamura, T., and Sakai, T. : Long-range Sonic Boom Prediction Considering Atmospheric Effects, InterNoise, 2011.

2.8) Stevens, S. S. : Perceived Level of Noise by Mark VII and Decibels (E), J. Acoust. Soc. Am., 51 (1972), pp. 575-601.

2.9) Hashimoto, A., Murakami, K., Aoyama, T., and Lahur, P. : Lift and Drag Prediction Using Automatic Hexahedra Grid Generation Method, 47th AIAA Aerospace Sciences Meeting, AIAA Paper 2009-1365, 2009.

2.10) Hashimoto, A., Murakami, K., Aoyama, T., Ishiko, K., Hishida, M., Sakashita, M., and Lahur, P. R. : Toward the Fastest Unstructured CFD Code 'FaSTAR', 50th AIAA Aerospace Sciences Meeting including the New Horizons Forum and Aerospace Exposition, AIAA 2012-1075, 2012.

2.11) Raymer, D. P. : Aircraft Design: A Conceptual Approach, 4th edition, AIAA Education Series, AIAA, 2006.

3.1) Ueno, A., Noguchi, M., and Makino, Y., : Aft-Boom Shaping for Small Supersonic Transport and Validation by Wind Tunnel Test, 48th Fluid Dynamics Conference/34th Aerospace Numerical Simulation Symposium, 2016. (in Japanese)
3.2) Li,W., and Rallabhandi, S. : Inverse Design of Low-Boom Supersonic Concepts Using Reversed Equivalent-Area Targets, Journal of Aircraft, 51, 1 (2014), pp. 29–36.

4.1) Ueno, A., Watanabe, Y., and Asako, T. : Conceptual design of silent supersonic transport considering airframe/propulsion integration, Proceedings of the 50th Aircraft Symposium, 2012. (in Japanese)
4.2) Lighthill, M. J., : Jet Noise, AIAA Journal, 1, 7 (1963), pp. 1507-1517.
4.3) Ueno A. and Watanabe Y. : Simultaneous Optimization of Airframe and Engine for Supersonic Transport, 28th International Congress of the Aeronautical Sciences, 2012.
4.4) Ueno, A. and Watanabe, Y. : Multidisciplinary Design Optimization of Engine Layout for Supersonic Airliner. Koku-Uchu-Gijyutsu (Aerospace Technology Japan, the Japan Society for Aeronautical and Space Sciences), 14 (2015), pp. 67-76. (in Japanese)
4.5) Ueno, A., Watanabe, Y., Salah El Din, I., Grenon, R., And Carrier, G. : Low Boom/Low Drag Small Size Supersonic Aircraft Design, VII European Congress on Computational Methods in Applied Sciences and Engineering (ECCOMAS Congress 2016), 2016.
4.6) Watanabe, Y., : Aerodynamic design of 3.5th configuration air intake for silent supersonic technology demonstrator S3TD, JAXA RM-08-019, 2009. (in Japanese)
4.7) Jones, D. R. : A Taxonomy of Global Optimization Methods Based on Response Surfaces, Journal of Global Optimization, 21 (2001), pp. 345-383.
4.8) Campbell, R. and Kremzier, E. : Performance of Wedge-type Boundary Layer Diverters, NACA RM E54C23, 1954.

JAXA Research and Development Memorandum JAXA-RM-18-001E

Low-Boom and Low-Drag Design of Small Supersonic Transport Considering Propulsion Airframe Integration

Edited and Published by: Japan Aerospace Exploration Agency
7-44-1 Jindaiji-higashimachi, Chofu-shi, Tokyo 182-8522 Japan
URL: http://www.jaxa.jp/
Date of Issue: October 3, 2018
Produced by: Matsueda Printing Inc.